

# Optimized Copper-Modified Zinc Oxide Photoanodes for Solar-to-Hydrogen Evolution

Premrudee Promdet,\* Fan Cui, Raul Quesada-Cabrera, Sanjayan Sathasivam, Jiang Wu, Claire J. Carmalt, and Ivan P. Parkin\*



Cite This: *ACS Appl. Mater. Interfaces* 2026, 18, 5061–5068



Read Online

ACCESS |

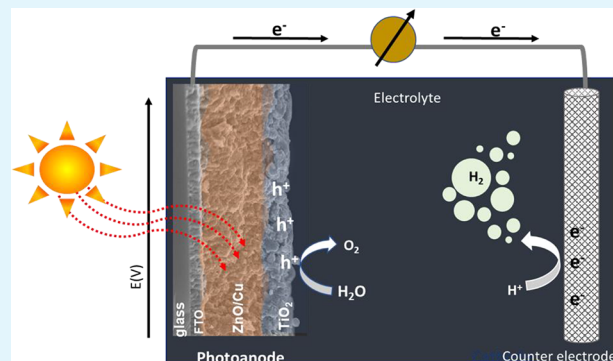
Metrics & More

Article Recommendations

Supporting Information

**ABSTRACT:** This work presents a single-step method for producing cost-efficient copper-modified zinc oxide photoanodes through scalable chemical vapor deposition. The role of Cu incorporation is thoroughly investigated, with the identification of an optimized loading of the metal in these films. The optimally Cu-modified ZnO sample (CZO-5.6) achieved a stable photocurrent of approximately  $1.22 \text{ mA cm}^{-2}$  at  $1.23 \text{ V}_{\text{RHE}}$  along with a Faradaic efficiency of 89%. This enhanced performance was attributed to surface plasmon resonance (SPR) effects induced by copper nanoparticles, as evidenced by photoluminescence spectroscopy results. To promote stability under the experimental conditions of the PEC cell, the best-performing photoanode was further protected using amorphous  $\text{TiO}_2$  deposited by atomic layer deposition. Amorphous  $\text{TiO}_2$  coatings have been found to be exceptionally stable in alkaline solutions and highly conductive for photogenerated holes, offering a promising solution for PEC electrode protection. This work not only describes a method for fabricating photoanodes with high photocatalytic activity but also suggests a low-cost route toward the development of photocatalysts for hydrogen production.

**KEYWORDS:** photoelectrochemical hydrogen evolution, copper-modified zinc oxide, plasmonic photocatalysts, cost-efficient photoanodes, chemical vapor deposition



## INTRODUCTION

Photoelectrochemical (PEC) water splitting is a promising route to sustainable hydrogen production, offering a direct method to convert solar energy into chemical fuel.<sup>1</sup> In a typical PEC cell, a photoanode (i.e., a light-absorbing semiconductor electrode) is immersed in an electrolyte and illuminated to drive the oxygen evolution reaction (OER).<sup>2</sup> This is paired with a counter electrode, typically platinum, which catalyzes the hydrogen evolution reaction (HER). While the HER is well understood and efficiently catalyzed under most conditions, overall water splitting is limited by the sluggish kinetics of the OER. An efficient HER can only proceed if the OER occurs at a comparable rate; however, the OER involves complex four-electron transfers and multiple proton-coupled steps, making it inherently more challenging.<sup>1–3</sup> As such, substantial research has focused on developing photoanode materials that enhance OER performance by improving light absorption, charge separation, and interfacial charge transfer.<sup>3,4</sup>

Various semiconductors, such as  $\text{TiO}_2$  and  $\text{Fe}_2\text{O}_3$ , have been explored as photoanodes.<sup>5–7</sup> Among them, zinc oxide ( $\text{ZnO}$ ) is particularly attractive due to its wide band gap (3.37 eV); suitable valence band position for water oxidation; and advantages in abundance, sustainability, and low cost.<sup>8</sup>  $\text{ZnO}$  also exhibits exceptionally high electron mobility (up to 100

times greater than that of  $\text{TiO}_2$ ), which facilitates effective separation of photogenerated charge carriers, thereby suppressing recombination and enhancing photocurrent generation. Its high surface reactivity further promotes interfacial redox processes.

Despite these advantages,  $\text{ZnO}$  is photoactive only under UV light, which constitutes only ~4% of the solar spectrum. It is also prone to photocorrosion in aqueous environments under illumination.<sup>9,10</sup> These drawbacks have motivated a wide range of material engineering strategies to enhance  $\text{ZnO}$ 's PEC performance, including doping to tune its electronic structure, heterojunction formation to improve charge separation, and surface modification with plasmonic metals to expand light harvesting into the visible region.

Among these, plasmonic modification has proven to be especially promising. When illuminated, plasmonic metal nanoparticles exhibit surface plasmon resonance (SPR),

Received: September 5, 2025

Revised: December 29, 2025

Accepted: December 29, 2025

Published: January 10, 2026



**Table 1. Physical and Functional Parameters of Pure ZnO and CZO Films with Varying Cu Contents (at %)<sup>a</sup>**

sample	[Cu]/at %	lattice parameters			thickness/nm	SA/ $\mu\text{m}^2$	$J/\text{mA cm}^{-2}$
		$a, b$ (Å)	$c$ (Å)	$V$ (Å $^3$ )			
CZO-0	0	3.25216	5.21218	47.74	1020 $\pm$ 36	25 $\pm$ 1	0.32
CZO-2.2	2.2	3.25481	5.21757	47.87	1150 $\pm$ 55	29 $\pm$ 3	0.55
CZO-3.7	3.7	3.25658	5.20835	47.84	990 $\pm$ 80	26 $\pm$ 2	0.74
CZO-5.6	5.6	3.25564	5.2164	47.88	1100 $\pm$ 20	29 $\pm$ 4	1.22
CZO-15.2	15.2	3.25569	5.21012	47.83	1050 $\pm$ 15	31 $\pm$ 3	0.60
TiO <sub>2</sub> @CZO-5.6	5.6	3.25564	5.2164	47.88	1150 $\pm$ 25	27 $\pm$ 2	1.43

<sup>a</sup>Physical data include lattice parameters and unit cell volume ( $V$ ), film thickness, and surface area (SA). Photocurrent density ( $J$ ) was obtained at 1.23 V<sub>RHE</sub>.

generating intense local electric fields and energetic hot carriers. In metal/n-type semiconductor systems, hot electrons with sufficient energy can overcome the Schottky barrier at the interface and be injected into the conduction band of the semiconductor, contributing to the photocurrent.<sup>11,12</sup> Simultaneously, hot holes left behind on the metal or photogenerated holes in the semiconductor drive the OER. SPR-induced effects also enhance light absorption and promote spatial charge separation, both of which are beneficial for PEC performance.

Noble metals such as Au, Ag, and Pt have been widely studied for their SPR effects in PEC systems.<sup>13–16</sup> However, several earth-abundant non-noble metals also exhibit SPR and can similarly improve the PEC activity. Among these, copper (Cu) is particularly attractive due to its large extinction cross section, photosensitivity, high conductivity, and low cost.<sup>11,17</sup>

Previous studies on Cu–ZnO systems have primarily focused on substitutional Cu doping to form solid solutions or on CuO–ZnO and Cu<sub>2</sub>O–ZnO composites.<sup>18–21</sup> For systems involving metallic Cu, the typical approach involves a two-step process: ZnO nanostructures are first synthesized via solvothermal methods, followed by Cu deposition using electrodeposition or physical vapor deposition (PVD).<sup>22,23</sup> These systems have largely been explored for electrocatalysis (e.g., nitrate-to-ammonia conversion) or thermal catalysis (e.g., CO<sub>2</sub> hydrogenation), rather than for PEC water splitting.<sup>22,23</sup>

To harness the plasmonic properties of Cu nanoparticles (NPs) for PEC applications, this study presents a single-step synthesis of Cu-modified ZnO photoanodes by using aerosol-assisted chemical vapor deposition (AACVD) under a nitrogen atmosphere. This scalable approach enables precise tuning of film properties by adjusting precursor chemistry, solvent, and deposition parameters.<sup>24–28</sup> The influence of Cu incorporation was systematically investigated, and an optimal Cu loading was identified for maximizing PEC hydrogen production. To improve stability under operational conditions, the best-performing photoanode was coated with amorphous TiO<sub>2</sub> via atomic layer deposition (ALD). Amorphous TiO<sub>2</sub> has demonstrated excellent stability in alkaline environments and high hole conductivity, making it an effective protective layer for PEC electrodes.<sup>29,30</sup>

## EXPERIMENTAL SECTION

All chemical precursors were used as received from Sigma-Aldrich. Cu-modified ZnO films were deposited from copper acetate monohydrate (99%) and zinc acetate dihydrate (98%) in methanol (99.8%) using aerosol-assisted chemical vapor deposition (AACVD). In this system (Scheme S1), an ultrasonic humidifier (Johnson Matthey) created a mist from the precursor mixtures, which was carried into a cold-wall reactor under a nitrogen flow (BOC, 1.0 l min<sup>-1</sup>). The products were deposited onto fluorine-doped tin oxide (FTO) silica-barrier float glass

substrates (cleaned using distilled water/detergent mix, isopropyl alcohol, and finally acetone before drying in a 70 °C oven) from NSG Pilkington Ltd. at 400 °C. The resulting films were adherent and passed the conventional Scotch tape test. A series of samples was prepared from precursor solutions containing a fixed concentration of zinc acetate (0.05 M) and varying concentrations of copper acetate (0, 10<sup>-3</sup>, 2·10<sup>-3</sup>, 4·10<sup>-3</sup>, 8·10<sup>-3</sup> M, respectively) in a total volume of 60 mL. In specific samples, a ~7 nm TiO<sub>2</sub> protective layer was deposited from titanium isopropoxide using atomic layer deposition (Ultratech, Savannah G2 S200) at 100 °C and a deposition rate of 0.48 Å per cycle.<sup>31</sup>

Film morphology and thickness were studied using top- and side-view scanning electron microscopy (SEM) on a JEOL6301 instrument operated at 10 kV. X-ray diffraction (XRD) analysis was carried out using a Bruker-AXS D8 (GADDS) diffractometer equipped with a monochromated Cu X-ray source emitting Cu K $\alpha$ 1 ( $\lambda$  = 1.54056 Å) and Cu K $\alpha$ 2 ( $\lambda$  = 1.54439 Å) radiation at an intensity ratio of 2:1 and a 2D area X-ray detector with a resolution of 0.01°. Films were analyzed under a glancing incidence angle ( $\theta$ ) of 1°. The diffraction patterns were refined using database standards. UV/vis spectroscopy was performed using a double monochromated PerkinElmer Lambda 950 UV/vis/NIR spectrophotometer in the 300–800 nm range. X-ray photoelectron spectroscopy (XPS) was performed using a Thermo K $\alpha$  spectrometer with monochromated Al K $\alpha$  radiation, a dual-beam charge compensation system, and a constant pass energy of 50 eV. Survey scans were collected over the range 0–1200 eV. High-resolution XPS spectra were acquired for the principal peaks of Zn (2p), Cu (2p), and Ti (2p) and fitted using CasaXPS software with the calibration of C 1s at 284.5 eV. Room temperature photoluminescence (Renishaw 1000) spectroscopy was employed to study the optical properties of the ZnO films using a He–Cd laser ( $\lambda$  = 325 nm,  $E$  = 3.8 eV). The surface roughness was characterized by atomic force microscopy (AFM) on a Keysight 5600LS scanning probe microscope, with a scan size of 5  $\mu\text{m}$   $\times$  5  $\mu\text{m}$ . High-resolution TEM (HR-TEM) was performed using a JEOL 2100 (200 kV) instrument fitted with a LaB<sub>6</sub> filament, giving a point resolution of 0.13 nm. The instrument was equipped with bright- and dark-field STEM detectors and an Oxford Instruments EDS detector.

Photoelectrochemical studies were conducted using a 0.5 M Na<sub>2</sub>SO<sub>4</sub> electrolyte solution (Fluka) at pH 7.0 in a three-electrode electrochemical cell, with Ag/AgCl and Pt serving as the reference and counter electrodes, respectively. The potential was controlled by a potentiostat (Ivium Technology), ranging from -1.0 to 1.23 V vs Ag/AgCl at a scan rate of 50 mV s<sup>-1</sup>. The photocurrent density ( $J$ ) and electric potential ( $V$ ) of the photoanode were measured by linear scanning voltammetry. Measurements were performed in the dark and under chopped and continuous illumination, respectively, using an Ivium Compact Stat lamp (Ivium Technologies). The emission spectrum of the lamp is shown in Figure S1 for reference. The irradiance of the lamp (100 mW cm<sup>-2</sup>, AM 1.5 G) was calibrated by using a silicon reference cell with an optical meter (Newport, Model 1918-R). Stability tests were conducted under AM 1.5 sun illumination in 0.5 M Na<sub>2</sub>SO<sub>4</sub> at pH 7.0, with a constant potential of 0.6 V vs RHE. Hydrogen generation in the PEC cell was monitored using gas chromatography (Shimadzu GC-2014) under a bias voltage of 0.6 V vs Ag/AgCl. The theoretical H<sub>2</sub> rate was obtained using eq 1.<sup>32</sup>

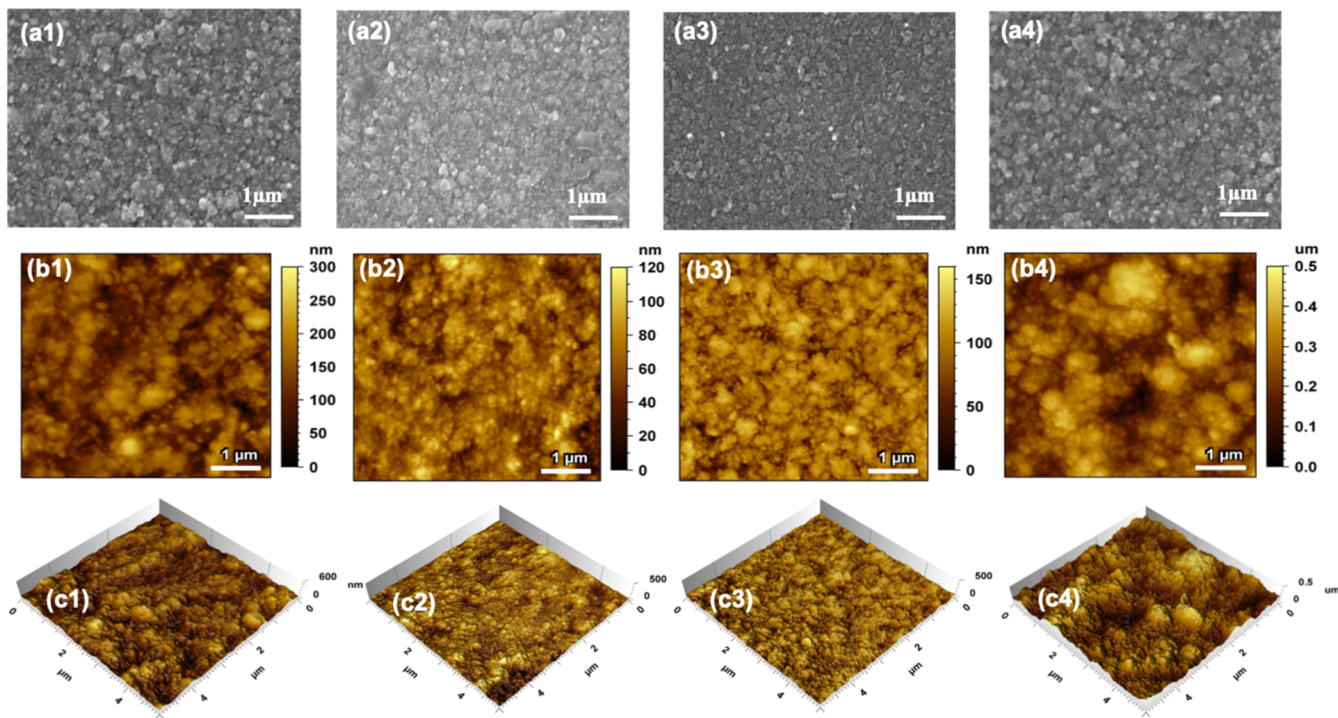


**Figure 1.** (a) Scanning electron microscopy (SEM) and (b, c) atomic force microscopy (AFM) images of the CZO films with increasing Cu content: (1) 2.2 at%, (2) 3.7 at%, (3) 5.6 at%, and (4) 15.2 at%. (b) and (c) 2D and 3D AFM images, respectively.

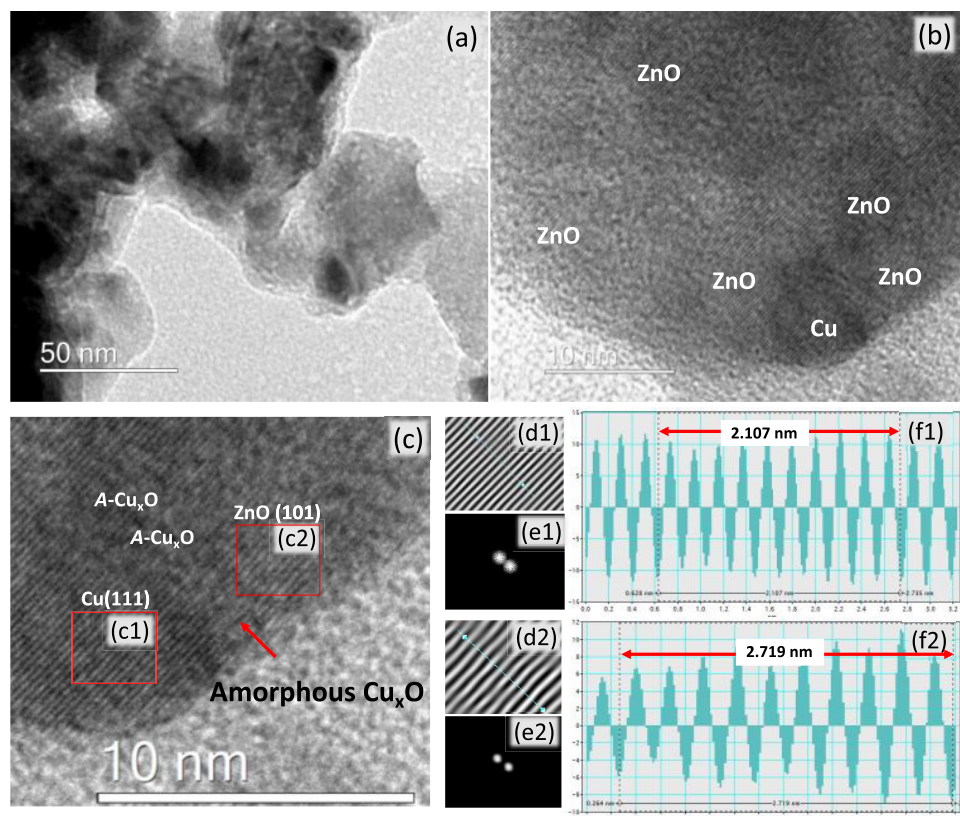


**Figure 2.** (a–c) High-resolution transmission electron microscopy (HR-TEM) images of sample CZO-5.6, highlighting Cu and ZnO areas and amorphous regions attributed to  $a\text{-Cu}_x\text{O}$ , (d) inverse fast Fourier transform (IFFT) transformation images, (e) fast Fourier transform (FFT) reciprocal-lattice image, and (f) corresponding lattice spacing line profile of the IFFT images of regions c1 and c2.

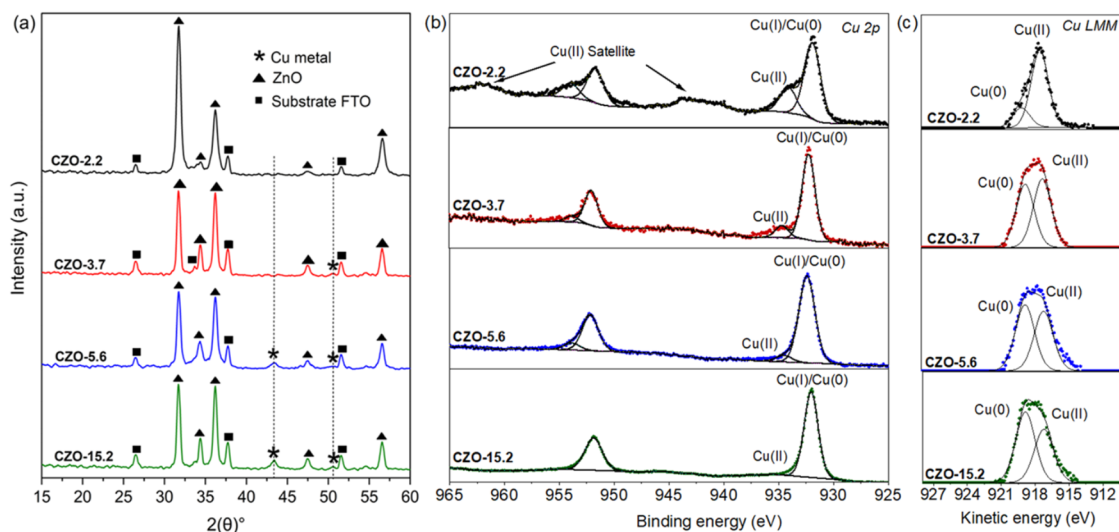


**Figure 3.** (a) XRD patterns of CZO films with varying Cu contents (2.2, 3.7, 5.6, and 15.2 at%, respectively). Triangle symbols correspond to wurtzite ZnO (JCPDS 00-036-1451), star symbols correspond to cubic Cu metal (JCPDS 65-9026), and square symbols correspond to the FTO substrate. (b) High-resolution XPS binding energies in the Cu 2p region and (c) corresponding Cu LMM spectra.

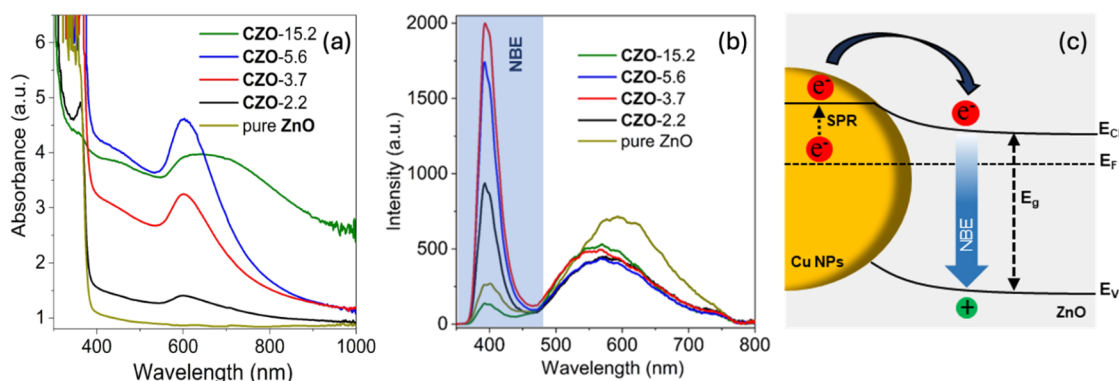


**Figure 4.** (a) Absorbance spectra of pure ZnO and CZO films, (b) corresponding photoluminescence spectra recorded under an excitation wavelength of 325 nm, and (c) schematic illustration of the energy band diagram of the CZO system showing the enhancement of near-band-edge (NBE) emission from hot electrons generated from the SPR effect.

$$H_2 = \frac{Q}{2F} = \frac{I \cdot t}{2F} = \frac{1}{2} \left( \int_0^t I dt \right) \quad (1)$$

where  $Q$  (units, C s) is the charge passing through the circuit during a period of  $t$  (units, s),  $I$  is the photocurrent, and  $F$  is the Faraday constant (96,484.34 C mol<sup>-1</sup>). The  $Q$  value is estimated by integrating the current over time when the current is not constant. The Faradaic efficiency, FE, was estimated from the ratio between experimental and theoretical  $H_2$  rates.

## RESULTS AND DISCUSSION

A series of Cu-modified ZnO films were deposited in a single step from methanolic mixtures of zinc acetate (0.05 M) and copper acetate (0, 10<sup>-3</sup>, 2·10<sup>-3</sup>, 4·10<sup>-3</sup>, 8·10<sup>-3</sup> M, respectively) using aerosol-assisted (AA) CVD (Figure S1) at 400 °C under a nitrogen atmosphere. Energy-dispersive X-ray spectroscopy (EDS) analysis showed the Cu content in the films to be 0, 2.2, 3.7, 5.6, and 15.2 at %, respectively, relative to Zn, thus increasing linearly with the increase in copper acetate concentration in the precursor solution. The films are henceforth referred to as CZO-(Cu at%), as listed in Table 1. EDS mapping analysis was also used to verify the uniform distribution of Cu in the samples (Figure S2). Scanning electron

microscopy (SEM) and atomic force microscopy (AFM) images showed that the films consisted of spherical particles with diameters ranging from 50 to 100 nm (Figure 1). Clustering of these particles into larger features, several hundred nanometers in width, was also observed across all films, with the effect most pronounced in the CZO-15.2 sample. The consistency in film morphology and surface area across the five CZO films is advantageous, as it allows us to dismiss any significant difference in performance to be due to variations in surface area.

High-resolution TEM analysis (Figure 2) also confirmed that the films were composed of particles with diameters up to 100 nm. The images clearly show crystal lattice fringes characteristic of metallic Cu, surrounded by amorphous or highly disordered copper oxide material, and, at a longer range, the crystalline ZnO host. The lattice spacing in the nanoparticle was 0.210 nm, corresponding to the (111) plane of Cu.<sup>33,34</sup> Interplanar spacing values of 0.271 nm were attributed to the (002) planes of hexagonal ZnO.

XRD analysis confirmed the formation of hexagonal wurtzite ZnO in all samples, with additional peaks corresponding to cubic metallic Cu appearing in films containing 3.7 atom % Cu and above (Figure 3a). It is important to note that metallic Cu may also be present at lower doping levels but in quantities too small

to be detected by XRD. The Le Bail fitting of the data was carried out to assess the impact of Cu doping on ZnO unit cell parameters (Table 1). However, due to the similar ionic radii of Zn(II) and Cu(II) (0.74 and 0.73 Å, respectively), no significant structural differences were observed.

Further characterization was carried out using XPS (Figure 3b), with the identification of surface Cu(0) metal centers and Cu(II) ions ( $2p_{3/2}$  peaks at 932.6 and 934.7 eV, respectively). It is worth noting that the area of the Cu(0) peak increased relative to that of the Cu(II) peak upon increasing the Cu content, as it corresponds to the growth of metal nanoparticles on the film surfaces. Likewise, the Cu LMM Auger peak attributed to the kinetic energy of Cu(0) at 918.2 eV increased relative to that of Cu(II) at 917.2 eV upon increasing the Cu content in the films (Figure 3c). The presence of surface Cu(II) species supports the identification of amorphous/disordered copper oxide (A-CuO), as noted in the HR-TEM studies.

The formation of Cu NPs had a notable impact on the optical properties of the films (Figure 4a), with an absorption band emerging at *ca.* 580 nm upon increasing the Cu content. A red shift and broadening of this band in sample CZO-15.2 correlated with the growth of large, aggregated particles and is consistent with previous observations of surface plasmon resonance (SPR) from Cu NPs.<sup>36</sup>

Photoluminescence (PL) studies showed typical bands in the UV (near-band-edge, NBE) and visible regions (Figure 4b). The NBE of ZnO is usually located within 368–380 nm, which is due to the radiative recombination of free excitons.<sup>37</sup> In our case, the NBE was red-shifted to  $\sim$ 390 nm likely due to surface defects, which are commonly observed for ZnO.<sup>38</sup> Surface defects can induce band bending, effectively reducing the band gap near the surface and contributing to charge recombination at lower energies compared to those in the bulk, hence a red shift of the NBE band.<sup>39</sup> These recombination centers would also contribute to the quenching of NBE emission, as observed for the nominally pure ZnO in our studies, with a weak NBE band relative to the features in the visible region (Figure 4b). The broad band in the visible region (450–750 nm) is typically assigned to luminescence due to structural defects.<sup>40</sup> Doping or passivation of surface states associated with deep-level defects (i.e., oxygen vacancies, zinc interstitials, etc.) upon incorporation of Cu can lead to emission from shallow defect levels, inducing a blue shift in the visible emission, as observed in the case of the CZO films (Figure 4b). It is interesting to note that the NBE peak in the CZO films was not shifted relative to that in pure ZnO. The formation of a Schottky barrier upon the deposition of Cu NPs would lead to changes in the local band structure near the surface, which is expected to shift the NBE emission from interfacial regions; however, this effect may not be significant enough to affect bulk emission.<sup>41</sup> Cu doping was too low and likely well dispersed to induce significant changes in the bulk electronic structure. Defect passivation can counterbalance band bending or carrier concentration effects that contribute to maintaining the NBE energy; however, it can have an impact on band intensity. Fewer surface defects per unit volume would reduce nonradiative recombination centers at the surface and thus increase NBE band intensity,<sup>42</sup> which is expected upon increasing Cu loading. This is the case observed for CZO films with low Cu contents (CZO-2.2, CZO-3.7), as shown in Figure 4b, where the NBE band intensity increases. At the same time, large Cu NPs can act as recombination centers or contribute to interfacial defects, potentially decreasing the NBE band intensity (CZO-15.2). It is worth noting that the

plasmonic coupling from Cu NPs can also impact the NBE band intensity, following a similar nonlinear correlation: too-small NPs result in poor field enhancement and thus weak SPR, while too-large NPs can lead to radiative damping and scattering, decreasing field enhancement again. The strongest NBE intensities recorded corresponded to samples CZO-3.7 and CZO-5.6 (Figure 4b). An enhanced NBE emission has been attributed to SPR upon injection of hot electrons from metal NPs into the conduction band of semiconductors (Figure 4c).<sup>43,44</sup> Some authors have demonstrated an SPR effect in Cu NPs deposited on titania ( $TiO_2$ ) substrates after prolonged exposure to air oxidation.<sup>45</sup> Charge transfer from Cu NPs into ZnO has also been demonstrated through an amorphous CuO layer, resulting in an enhancement of photocatalytic performance.<sup>44,46</sup>

The CZO films were assessed as photoanodes in a three-electrode electrochemical cell using a 0.5 M  $Na_2SO_4$  electrolyte solution at pH 7.0. Figure 5 shows current–voltage ( $J$ – $V$ )

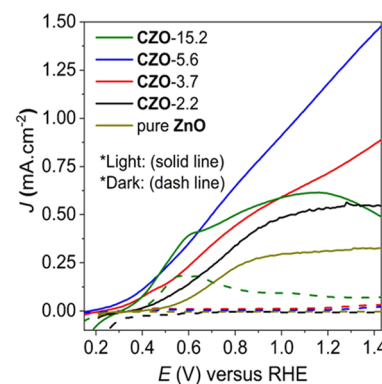


**Figure 5.** Photoelectrochemical properties of pure ZnO and CZO photoanodes providing  $J$ – $V$  curves obtained in the dark and under AM 1.5 G illumination.

curves in the dark and under simulated sunlight conditions (AM = 1.5 G,  $100 \text{ mW cm}^{-2}$ ). The onset potential of these films shifted cathodically compared with that of pure ZnO, ranging from  $\sim$ 0.55  $V_{RHE}$  (CZO-0) to  $\sim$ 0.35  $V_{RHE}$  (CZO-15.2), indicating an enhanced performance of the Cu-modified photoanodes.<sup>47</sup> The corresponding current densities are given in Table 1, following an almost linear trend with Cu loading. The best performance was obtained from sample CZO-5.6, reaching *ca.*  $1.22 \text{ mA cm}^{-2}$  (at  $1.23 V_{RHE}$ ). This is in line with previous reports demonstrating enhanced photocatalytic properties upon incorporation of Cu into ZnO materials.<sup>48,49</sup> The stability of the CZO-15.2 sample was compromised at high voltages, as inferred from an inspection of Figure 5.

Further work explored strategies to improve the stability of the photoanodes, as they exhibited corrosion within 1 h under the conditions used in these experiments (0.1  $V_{Ag/AgCl}$  AM 1.5 G). In particular, a thin amorphous  $TiO_2$  protective coating was deposited onto the best-performing photoanode (i.e., sample CZO-5.6) by using atomic layer deposition. An optimal thickness of 7 nm with respect to effective levels of protection and hole transfer was chosen using guidance from previous studies in the literature for PEC electrodes.<sup>29,30</sup> The presence of  $TiO_2$  was confirmed by EDS analysis, and the dominant  $Ti 2p_{3/2}$  peak was identified at 458.4 eV in XPS analysis (Figure S2). XRD studies showed no indication of crystalline  $TiO_2$  phases after deposition. As shown in Figure 6a, the  $TiO_2$  layer

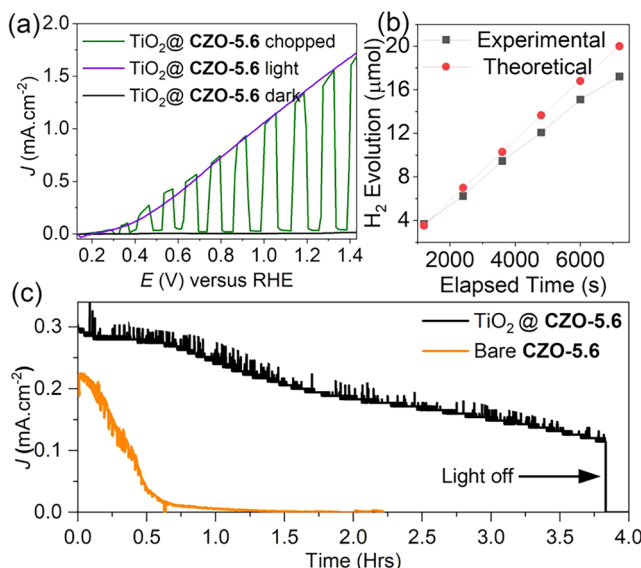


**Figure 6.** (a) Photocurrent density–voltage curves obtained from sample  $\text{TiO}_2$ @CZO-5.6 under dark, light, and chopped AM 1.5 G illumination. (b) Corresponding experimental and theoretical  $\text{H}_2$  rates under continuous illumination (AM 1.5 G  $100 \text{ mW cm}^{-2}$ ) with a bias voltage of  $0.6 \text{ V}_{\text{Ag/AgCl}}$ . (c) Stability of bare CZO-5.6 and  $\text{TiO}_2$ @CZO-5.6 samples measured with a bias of  $0.5 \text{ V}_{\text{RHE}}$  under AM 1.5 G sun illumination.

contributed to the photocurrent density of the film, improving its performance to  $1.43 \text{ mA cm}^{-2}$  at  $1.23 \text{ V}_{\text{RHE}}$ , with a photocurrent onset potential of  $\sim 0.35 \text{ V}_{\text{RHE}}$ . This result is significantly higher than that of other Zn-based anodic materials reported in the literature (Table 2). The enhanced photocatalytic activity upon deposition of an amorphous  $\text{TiO}_2$  coating has been attributed to a facile transfer of holes across the semiconductor–electrolyte interface.<sup>50</sup> This strategy also increased the stability of the photoanode by tenfold, with a useful half-life of  $\sim 3 \text{ h}$  (Figure 6b). The extent of corrosion after that time was evaluated by monitoring the Cu(II) satellite peak in XPS (Figure S3), with the formation of CuO and a concomitant color change from green to dark yellow.

The  $\text{H}_2$  generated from the optimized photoanode,  $\text{TiO}_2$ @CZO-5.6, under a bias of  $0.6 \text{ V}_{\text{Ag/AgCl}}$  and AM 1.5 sun illumination, increased linearly and fitted the theoretical value, as shown in Figure 6c. The photoanode exhibited a high and stable Faradaic efficiency of 89% for the 45 min duration of the stability test, indicating that the surface conditions promoted carriers to participate in the water-splitting reaction.

**Table 2. Comparison of Photocurrent Densities ( $J$ , at 1.3 V) from Different ZnO-Based Electrodes Reported in the Literature and This Work<sup>a</sup>**

photoelectrode	deposition method	$J / \text{mA cm}^{-2}$	RE	refs
ZnO nanostructure	thermal oxidation, magnetron sputtering	0.05	$\text{Ag/AgCl}$	51
ZnO nanostructure	pulsed laser deposition	0.20	$\text{Ag/AgCl}$	52
ZnO plate film	electrodeposition	0.4	RHE	53
N-doped ZnO wire	hydrothermal deposition + annealing	0.5	$\text{Ag/AgCl}$	54
graphene-ZnO	alkali precipitation + solvothermal	0.6	$\text{Ag/AgCl}$	55
defect-rich ZnO rods	microwave-assisted chemical bath	0.705	RHE	56
ZnO nanostructure	solution processing + dip-coating	1.00	RHE	57
$\text{TiO}_2$ @Cu-ZnO film	chemical vapor deposition	1.43	RHE	this work

<sup>a</sup>It is important to note that the testing conditions (e.g., electrolyte composition, pH, and reference electrode) are not identical across all tests. Please see the references for further information.

## CONCLUSIONS

Cost-efficient, optimized Cu-modified ZnO films synthesized by using chemical vapor deposition methods were used as photoanodes for solar-to-hydrogen evolution. The incorporation of Cu nanoparticles enhanced the photocatalytic properties of the photoanode, which was mainly attributed to surface plasmon resonance (SPR) effects, based on absorbance and photoluminescence evidence. The addition of an amorphous  $\text{TiO}_2$  protective coating to the best-performing film significantly enhanced its photocurrent density above average reported in the literature. The protective coating contributed to a substantial extension (tenfold) of the useful life of the photoanode. This encouraging result represents a step forward in the fabrication of optimized photoanodes for green  $\text{H}_2$  generation, and it underscores the need for the implementation of synthesis strategies for high-surface-area photoanodes.

## ASSOCIATED CONTENT

### Data Availability Statement

Data for this article are available upon request from the corresponding authors.

### Supporting Information

The Supporting Information is available free of charge at <https://pubs.acs.org/doi/10.1021/acsami.5c17721>.

Film growth setup, spectral irradiance of the AM 1.5 G standard solar spectrum, and additional material characterization (PDF)

## AUTHOR INFORMATION

### Corresponding Authors

Premrudee Promdet – Materials Chemistry Centre, Department of Chemistry, UCL (University College London), London WC1H 0AJ, U.K.; [orcid.org/0000-0002-4509-523X](https://orcid.org/0000-0002-4509-523X); Email: [premrudee.promdet.17@ucl.ac.uk](mailto:premrudee.promdet.17@ucl.ac.uk)

Ivan P. Parkin – Materials Chemistry Centre, Department of Chemistry, UCL (University College London), London WC1H 0AJ, U.K.; [orcid.org/0000-0002-4072-6610](https://orcid.org/0000-0002-4072-6610); Email: [i.p.parkin@ucl.ac.uk](mailto:i.p.parkin@ucl.ac.uk)

### Authors

Fan Cui – Department of Electronic & Electrical Engineering, UCL (University College London), London WC1E 7JE, U.K.

Raul Quesada-Cabrera – Materials Chemistry Centre, Department of Chemistry, UCL (University College London), London WC1H 0AJ, U.K.; Department of Chemistry, Institute

of Environmental Studies and Natural Resources (i-UNAT), Universidad de Las Palmas de Gran Canaria (ULPGC), Las Palmas 35017, Spain

**Sanjayan Sathasivam** – Materials Chemistry Centre, Department of Chemistry, UCL (University College London), London WC1H 0AJ, U.K.; School of Engineering & Design, London South Bank University, London SE1 0AA, U.K.; Energy, Materials & Environment Research Centre, London South Bank University, London SE1 0AA, U.K.;  [orcid.org/0000-0002-5206-9558](https://orcid.org/0000-0002-5206-9558)

**Jiang Wu** – Institute of Fundamental and Frontier Sciences, University of Electronic Science and Technology of China, Chengdu 610054, P. R. China;  [orcid.org/0000-0003-0679-6196](https://orcid.org/0000-0003-0679-6196)

**Claire J. Carmalt** – Materials Chemistry Centre, Department of Chemistry, UCL (University College London), London WC1H 0AJ, U.K.;  [orcid.org/0000-0003-1788-6971](https://orcid.org/0000-0003-1788-6971)

Complete contact information is available at:

<https://pubs.acs.org/10.1021/acsami.5c17721>

## Notes

The authors declare no competing financial interest.

## ACKNOWLEDGMENTS

This work was supported by the Development and Promotion of Science and Technology Talents Project with an awarded fellowship to PP. RQC thanks the Spanish Ministry of Science and Innovation (MCI) and the Next Generation EU/PRTR program for grant PID2022-143294OB-I00. IPP and CJC thank EPSRC for grant EP/L0177709/1. SS thanks the School of Engineering and Design, LSBU, and the Energy, Materials & Environment Research Centre, LSBU for funding.

## REFERENCES

- (1) Dong, G.; Yan, L.; Bi, Y. Advanced Oxygen Evolution Reaction Catalysts for Solar-Driven Photoelectrochemical Water Splitting. *J. Mater. Chem. A Mater.* **2023**, *11* (8), 3888–3903.
- (2) Jiang, C.; Moniz, S. J. A.; Wang, A.; Zhang, T.; Tang, J. Photoelectrochemical Devices for Solar Water Splitting—Materials and Challenges. *Chem. Soc. Rev.* **2017**, *46* (15), 4645–4660.
- (3) Hisatomi, T.; Kubota, J.; Domen, K. Recent Advances in Semiconductors for Photocatalytic and Photoelectrochemical Water Splitting. *Chem. Soc. Rev.* **2014**, *43* (22), 7520–7535.
- (4) Xing, X.; Gao, Q.; Feng, C.; Zhou, Z.; Liu, X.; Guo, Y.; Zhang, J.; Du, J.; Zhang, H. Interfacial Engineering Induced Charge Accumulation for Enhanced Solar Water Splitting. *Adv. Funct. Mater.* **2025**, No. e19825.
- (5) Zhou, Z.; Wang, Y.; Li, L.; Yang, L.; Niu, Y.; Yu, Y.; Guo, Y.; Wu, S. Constructing a Full-Space Internal Electric Field in a Hematite Photoanode to Facilitate Photogenerated-Carrier Separation and Transfer. *J. Mater. Chem. A Mater.* **2022**, *10* (15), 8546–8555.
- (6) Zhou, Z.; Wu, K.; Liu, X.; Ma, S.; Yu, Y.; Wang, P.; Guo, Y.; Zhang, X.; Fan, Y.; Du, J. Integrating Dual-MOFs Heterojunction onto Hematite Photoanode for Boosting Photogenerated Carrier Separation. *Chem. Eng. J.* **2025**, *S20*, No. 166418.
- (7) Xing, X.; Zeng, X.; Wu, S.; Song, P.; Song, X.; Guo, Y.; Li, Z.; Li, H.; Zhou, Z.; Du, J. Constructing Metal–Organic Framework Films with Adjustable Electronic Properties on Hematite Photoanode for Boosting Photogenerated Carrier Transport. *Small* **2024**, *20* (46), No. 2404438.
- (8) Kang, Z.; Si, H.; Zhang, S.; Wu, J.; Sun, Y.; Liao, Q.; Zhang, Z.; Zhang, Y. Interface Engineering for Modulation of Charge Carrier Behavior in ZnO Photoelectrochemical Water Splitting. *Adv. Funct. Mater.* **2019**, *29* (15), No. 1808032.
- (9) Bae, H. S.; Yoon, M. H.; Kim, J. H.; Im, S. Photodetecting Properties of ZnO-Based Thin-Film Transistors. *Appl. Phys. Lett.* **2003**, *83* (25), 5313–5315.
- (10) Chandiran, A. K.; Abdi-Jalebi, M.; Nazeeruddin, M. K.; Grätzel, M. Analysis of Electron Transfer Properties of ZnO and TiO<sub>2</sub> Photoanodes for Dye-Sensitized Solar Cells. *ACS Nano* **2014**, *8* (3), 2261–2268.
- (11) Mascaretti, L.; Dutta, A.; Kment, Š.; Shalaev, V. M.; Boltasseva, A.; Zboril, R.; Naldoni, A. Plasmon-enhanced Photoelectrochemical Water Splitting for Efficient Renewable Energy Storage. *Adv. Mater.* **2019**, *31* (31), No. 1805513.
- (12) Zhang, Y.; Guo, W.; Zhang, Y.; Wei, W. D. Plasmonic Photoelectrochemistry: In View of Hot Carriers. *Adv. Mater.* **2021**, *33* (46), No. 2006654.
- (13) Zeng, H.; Peisheng, L.; Weiping, C.; Shikuan, Y.; Xiaoxia, X. Controllable Pt/ZnO Porous Nanocages with Improved Photocatalytic Activity. *J. Phys. Chem. C* **2008**, *112* (49), 19620–19624.
- (14) Wang, F.; Jiang, Y.; Lawes, D. J.; Ball, G. E.; Zhou, C.; Liu, Z.; Amal, R. Analysis of the Promoted Activity and Molecular Mechanism of Hydrogen Production over Fine Au-Pt Alloyed TiO<sub>2</sub> Photocatalysts. *ACS Catal.* **2015**, *5* (7), 3924–3931.
- (15) Naseri, N.; Kim, H.; Choi, W.; Moshfegh, A. Z. Implementation of Ag Nanoparticle Incorporated WO<sub>3</sub> Thin Film Photoanode for Hydrogen Production. *Int. J. Hydrogen Energy* **2013**, *38* (5), 2117–2125.
- (16) Yang, J.; Wang, D.; Han, H.; Li, C. Roles of Cocatalysts in Photocatalysis and Photoelectrocatalysis. *Acc. Chem. Res.* **2013**, *46* (8), 1900–1909.
- (17) Hassan, I. A.; Sathasivam, S.; Nair, S. P.; Carmalt, C. J. Antimicrobial Properties of Copper-Doped ZnO Coatings under Darkness and White Light Illumination. *ACS Omega* **2017**, *2* (8), 4556–4562.
- (18) Kale, G.; Arbus, S.; Kawade, U.; Kadam, S.; Nikam, L.; Kale, B. Paper Templated Synthesis of Nanostructured Cu–ZnO and Its Enhanced Photocatalytic Activity under Sunlight. *J. Mater. Sci.: Mater. Electron.* **2019**, *30* (7), 7031–7042.
- (19) Bai, J.; Li, Y.; Wang, R.; Huang, K.; Zeng, Q.; Li, J.; Zhou, B. A Novel 3D ZnO/Cu<sub>2</sub>O Nanowire Photocathode Material with Highly Efficient Photoelectrocatalytic Performance. *J. Mater. Chem. A Mater.* **2015**, *3* (45), 22996–23002.
- (20) Simon, Q.; Barreca, D.; Gasparotto, A.; Maccato, C.; Montini, T.; Gombac, V.; Fornasiero, P.; Lebedev, O. I.; Turner, S.; Van Tendeloo, G. Vertically Oriented CuO/ZnO Nanorod Arrays: From Plasma-Assisted Synthesis to Photocatalytic H<sub>2</sub> Production. *J. Mater. Chem.* **2012**, *22* (23), 11739–11747.
- (21) Deo, M.; Shinde, D.; Yengantiwar, A.; Jog, J.; Hannoyer, B.; Sauvage, X.; More, M.; Ogale, S. Cu<sub>2</sub>O/ZnO Hetero-Nanobrush: Hierarchical Assembly, Field Emission and Photocatalytic Properties. *J. Mater. Chem.* **2012**, *22* (33), 17055–17062.
- (22) Feng, A.; Hu, Y.; Yang, X.; Lin, H.; Wang, Q.; Xu, J.; Liu, A.; Wu, G.; Li, Q. ZnO Nanowire Arrays Decorated with Cu Nanoparticles for High-Efficiency Nitrate to Ammonia Conversion. *ACS Catal.* **2024**, *14* (8), 5911–5923.
- (23) Wu, W.; Wang, Y.; Luo, L.; Wang, M.; Li, Z.; Chen, Y.; Wang, Z.; Chai, J.; Cen, Z.; Shi, Y.; et al. CO<sub>2</sub> Hydrogenation over Copper/ZnO Single-atom Catalysts: Water-promoted Transient Synthesis of Methanol. *Angew. Chem., Int. Ed.* **2022**, *61* (48), No. e202213024.
- (24) Sun, L.; Yuan, G.; Gao, L.; Yang, J.; Chhowalla, M.; Gharahcheshmeh, M. H.; Gleason, K. K.; Choi, Y. S.; Hong, B. H.; Liu, Z. Chemical Vapour Deposition. *Nat. Rev. Methods Primers* **2021**, *1* (1), No. 5.
- (25) Chadwick, N.; Sathasivam, S.; Kafizas, A.; Bawaked, S. M.; Obaid, A. Y.; Al-Thabaiti, S.; Basahel, S. N.; Parkin, I. P.; Carmalt, C. J. Combinatorial Aerosol Assisted Chemical Vapour Deposition of a Photocatalytic Mixed SnO<sub>2</sub> <inf>2</inf> TiO<sub>2</sub> <inf>2</inf> Thin Film. *J. Mater. Chem. A Mater.* **2014**, *2* (14), 5108–5116, DOI: [10.1039/c4ta00545g](https://doi.org/10.1039/c4ta00545g).
- (26) Promdet, P.; Quesada-Cabrera, R.; Sathasivam, S.; Li, J.; Jiamprasertboon, A.; Guo, J.; Taylor, A.; Carmalt, C. J.; Parkin, I. P.

High Defect Nanoscale ZnO Films with Polar Facets for Enhanced Photocatalytic Performance. *ACS Appl. Nano Mater.* **2019**, *2* (5), 2881–2889.

(27) Sathasivam, S.; Arnepalli, R. R.; Kumar, B.; Singh, K. K.; Visser, R. J.; Blackman, C. S.; Carmalt, C. J. Solution Processing of GaAs Thin Films for Photovoltaic Applications. *Chem. Mater.* **2014**, *26* (15), 4419–4424.

(28) Li, J.; Sathasivam, S.; Taylor, A.; Carmalt, C. J.; Parkin, I. P. Single Step Route to Highly Transparent, Conductive and Hazy Aluminium Doped Zinc Oxide Films. *RSC Adv.* **2018**, *8* (74), 42300–42307.

(29) Hu, S.; Shaner, M. R.; Beardslee, J. A.; Lichterman, M.; Brunschwig, B. S.; Lewis, N. S. Amorphous TiO<sub>2</sub> Coatings Stabilize Si, GaAs, and GaP Photoanodes for Efficient Water Oxidation. *Science* **2014**, *344* (6187), 1005–1009.

(30) Yu, Y.; Zhang, Z.; Yin, X.; Kvit, A.; Liao, Q.; Kang, Z.; Yan, X.; Zhang, Y.; Wang, X. Enhanced Photoelectrochemical Efficiency and Stability Using a Conformal TiO<sub>2</sub> Film on a Black Silicon Photoanode. *Nat. Energy* **2017**, *2* (6), 1–7, DOI: 10.1038/nenergy.2017.45.

(31) Wilson, R. L.; Simion, C. E.; Blackman, C. S.; Carmalt, C. J.; Stanoi, A.; Di Maggio, F.; Covington, J. A. The Effect of Film Thickness on the Gas Sensing Properties of Ultra-Thin TiO<sub>2</sub> Films Deposited by Atomic Layer Deposition. *Sensors* **2018**, *18* (3), No. 735.

(32) Alotaibi, B.; Nguyen, H. P. T.; Zhao, S.; Kibria, M. G.; Fan, S.; Mi, Z. Highly Stable Photoelectrochemical Water Splitting and Hydrogen Generation Using a Double-Band InGaN/GaN Core/Shell Nanowire Photoanode. *Nano Lett.* **2013**, *13* (9), 4356–4361.

(33) Chen, C.; Hu, Z.; Li, Y.; Liu, L.; Mori, H.; Wang, Z. In-Situ High-Resolution Transmission Electron Microscopy Investigation of Overheating of Cu Nanoparticles. *Sci. Rep.* **2016**, *6*, 4–11.

(34) Zhang, Z.; Ji, Y.; Li, J.; Zhong, Z.; Su, F. Synergistic Effect in Bimetallic Copper-Silver (Cu<sub>x</sub>Ag) Nanoparticles Enhances Silicon Conversion in Rochow Reaction. *RSC Adv.* **2015**, *5* (67), 54364–54371.

(35) Du, X. W.; Fu, Y. S.; Sun, J.; Han, X.; Liu, J. Complete UV Emission of ZnO Nanoparticles in a PMMA Matrix. *Semicond. Sci. Technol.* **2006**, *21* (8), 1202–1206.

(36) Amendola, V.; Pilot, R.; Frasconi, M.; Maragò, O. M.; Iati, M. A. Surface Plasmon Resonance in Gold Nanoparticles: A Review. *J. Phys.: Condens. Matter* **2017**, *29* (20), No. 203002.

(37) Ischenko, V.; Polarz, S.; Grote, D.; Stavarache, V.; Fink, K.; Driess, M. Zinc Oxide Nanoparticles with Defects. *Adv. Funct. Mater.* **2005**, *15* (12), 1945–1954.

(38) McCluskey, M. D.; Jokela, S. J. Defects in ZnO. *J. Appl. Phys.* **2009**, *106* (7), No. 071101, DOI: 10.1063/1.3216464.

(39) Zhang, Z.; Yates, J. T., Jr Band Bending in Semiconductors: Chemical and Physical Consequences at Surfaces and Interfaces. *Chem. Rev.* **2012**, *112* (10), 5520–5551.

(40) Djurišić, A.; Choy, W. C. H.; Roy, V. A. L.; Leung, Y. H.; Kwong, C. Y.; Cheah, K. W.; Rao, T. K. G.; Chan, W. K.; Lui, H. F.; Surya, C. Photoluminescence and Electron Paramagnetic Resonance of ZnO Tetrapod Structures. *Adv. Funct. Mater.* **2004**, *14* (9), 856–864.

(41) Brillson, L. J.; Lu, Y. ZnO Schottky Barriers and Ohmic Contacts. *J. Appl. Phys.* **2011**, *109* (12), No. 121301, DOI: 10.1063/1.3581173.

(42) Raji, R.; Gopchandran, K. G. ZnO Nanostructures with Tunable Visible Luminescence: Effects of Kinetics of Chemical Reduction and Annealing. *J. Sci.: Adv. Mater. Devices* **2017**, *2* (1), 51–58.

(43) Khan, M. R.; Chuan, T. W.; Yousuf, A.; Chowdhury, M. N. K.; Cheng, C. K. Schottky Barrier and Surface Plasmonic Resonance Phenomena towards the Photocatalytic Reaction: Study of Their Mechanisms to Enhance Photocatalytic Activity. *Catal. Sci. Technol.* **2015**, *5* (5), 2522–2531.

(44) Shahine, I.; Jradi, S.; Beydoun, N.; Gaumet, J. J.; Akil, S. Plasmon-Enhanced Photoluminescence and Photocatalysis Reactions in Metal-Semiconductor Nanomaterials: UV-Generated Hot Electron in Gold-Zinc Oxide. *ChemPhotoChem* **2020**, *4* (3), 181–194.

(45) Zhao, S.; Cheng, Z.; Wang, S.; Hao, H.; Fang, Y. Maintaining the Localized Surface Plasmon Resonance of Copper Nanoparticles by Defective TiO<sub>2</sub> Thin Films. *Appl. Phys., A* **2021**, *127* (12), No. 930.

(46) Guidelli, E. J.; Baffa, O.; Clarke, D. R. Enhanced UV Emission from Silver/ZnO and Gold/ZnO Core-Shell Nanoparticles: Photoluminescence, Radioluminescence, and Optically Stimulated Luminescence. *Sci. Rep.* **2015**, *5*, No. 14004.

(47) Jang, J. W.; Friedrich, D.; Müller, S.; Lamers, M.; Hempel, H.; Lardhi, S.; Cao, Z.; Harb, M.; Cavallo, L.; Heller, R.; Eichberger, R.; van de Krol, R.; Abdi, F. F. Enhancing Charge Carrier Lifetime in Metal Oxide Photoelectrodes through Mild Hydrogen Treatment. *Adv. Energy Mater.* **2017**, *7* (22), No. 1701536.

(48) Dom, R.; Baby, L. R.; Kim, H. G.; Borse, P. H. Enhanced Solar Photoelectrochemical Conversion Efficiency of ZnO:Cu Electrodes for Water-Splitting Application. *Int. J. Photoenergy* **2013**, *2013*, 18–20.

(49) Alatawi, N. M.; Saad, L. B.; Soltane, L.; Moulahi, A.; Mjejr, I.; Sediri, F. Enhanced Solar Photocatalytic Performance of Cu-Doped Nanosized ZnO. *Polyhedron* **2021**, *197*, No. 115022.

(50) Hu, S.; Shaner, M. R.; Beardslee, J. A.; Lichterman, M.; Brunschwig, B. S.; Lewis, N. S. Amorphous TiO<sub>2</sub> coatings Stabilize Si, GaAs, and GaP Photoanodes for Efficient Water Oxidation. *Science* **2014**, *344* (6187), 1005–1009.

(51) Shet, S. Zinc Oxide (ZnO) Nanostructures for Photoelectrochemical Water Splitting Application. *ECS Meet. Abstr.* **2010**, No. 2, 135.

(52) Wolcott, A.; Smith, W. A.; Kuykendall, T. R.; Zhao, Y.; Zhang, J. Z. Photoelectrochemical Study of Nanostructured ZnO Thin Films for Hydrogen Generation from Water Splitting. *Adv. Funct. Mater.* **2009**, *19* (12), 1849–1856.

(53) Emin, S.; Fanetti, M.; Abdi, F. F.; Lisjak, D.; Valant, M.; Van De Krol, R.; Dam, B. Photoelectrochemical Properties of Cadmium Chalcogenide-Sensitized Textured Porous Zinc Oxide Plate Electrodes. *ACS Appl. Mater. Interfaces* **2013**, *5* (3), 1113–1121.

(54) Yang, X.; Wolcott, A.; Wang, G.; Sobo, A.; Fitzmorris, R. C.; Qian, F.; Zhang, J. Z.; Li, Y. Nitrogen-Doped ZnO Nanowire Arrays for Photoelectrochemical Water Splitting. *Nano Lett.* **2009**, *9*, 2331–2336.

(55) Tayebi, M.; Tayyebi, A.; Masoumi, Z.; Lee, B. K. Photocorrosion Suppression and Photoelectrochemical (PEC) Enhancement of ZnO via Hybridization with Graphene Nanosheets. *Appl. Surf. Sci.* **2020**, *502*, No. 144189.

(56) Commandeur, D.; Brown, G.; Hills, E.; Spencer, J.; Chen, Q. Defect-Rich ZnO Nanorod Arrays for Efficient Solar Water Splitting. *ACS Appl. Nano Mater.* **2019**, *2* (3), 1570–1578.

(57) Bora, D. K.; Braun, A. Solution Processed Transparent Nanoparticulate ZnO Thin Film Electrode for Photoelectrochemical Water Oxidation. *RSC Adv.* **2014**, *4* (45), 23562–23570.